Chapter 5
Feature-Based Registration Techniques

Cristian Lorenz, Tobias Klinder and Jens von Berg

Abstract In contrast to intensity-based image registration, where a similarity measure is typically evaluated at each voxel location, feature-based registration works on a sparse set of image locations. Therefore, it needs an explicit step of interpolation to supply a dense deformation field. In this chapter, the application of feature-based registration to pulmonary image registration as well as hybrid methods, combining feature-based with intensity-based registration, is discussed. In contrast to pure feature based registration methods, hybrid methods are increasingly proposed in the pulmonary context and have the potential to out-perform purely intensity based registration methods. Available approaches will be classified along the categories *feature type*, *correspondence definition*, and *interpolation type* to finally achieve a dense deformation field.

5.1 Introduction

Probably the most intuitive approach to find a suitable transformation bringing two images into the same frame of reference, is by means of a set of corresponding points. In principle, they could be defined manually. But since we want to define a non-rigid registration, needing perhaps hundreds or thousands of points for a decent deformation field, we will concentrate on automated procedures. We will discuss how suitable *feature* points can be found, how point correspondence in two images can be established, and how a transformation can finally be estimated. Still, we have a sparse point set in mind, associated with a specific feature, be it a vessel bifurcation or a characteristic gray value structure. This is in contrast to the so called *intensity based registration* which will be discussed in Chaps. 6 and 7. Intensity based image registration treats typically each image location equally. For every grid position or voxel in a source image, the corresponding location in a target image is found

C. Lorenz (✉) · T. Klinder · J. von Berg
Philips Research Laboratories, Hamburg, Germany
e-mail: cristian.lorenz@philips.com

J. Ehrhardt and C. Lorenz (eds.), *4D Modeling and Estimation of Respiratory Motion for Radiation Therapy*, Biological and Medical Physics, Biomedical Engineering,
DOI: 10.1007/978-3-642-36441-9_5,

by evaluating a suitable intensity based similarity measure. Most medical images, however, contain more or less homogeneous regions with no or little gray value contrast. This makes the above task of finding correspondence an ill-posed problem. It is commonly solved by either applying explicit smoothness constraints to the deformation field or by exploiting implicit smoothness introduced by the specific parameterization of the deformation field. In effect, the behavior of an intensity-based registration is mainly characterized by matching image regions with suitable contrast and performing an implicit or explicit interpolation in between.
The *feature-based* registration, however, explicitly attempts to register only highly structured image regions and to obtain a dense deformation field by interpolating the resulting sparse deformation vector field. A considerable variety of methods has been proposed, differing in feature type, and how feature correspondence is established. In addition, hybrid methods have been proposed, combining feature-based and intensity-based registration.
We classify feature-based registration algorithms based on the following categories:

- **Feature type**, which includes feature dimension (point, line, surface) and feature characterization (e.g. bifurcation-point, vessel-centerline, ridge-line of a surface, or other intensity patterns)
- **Feature correspondence definition** (e.g. anatomical labeling, 3D Shape Context, current-based, shaped-constrained deformable models)
- **Interpolation type** for generating dense deformation fields.

Consequently, the rest of this chapter is organized along these categories. Feature-based registration was very frequently used to estimate rigid or affine transformations. Here, we focus on non-linear transformations, for which feature-based registration was pioneered for the purpose of brain registration. In the context of a comparison of algorithms for pulmonary image registration, performed at a satellite workshop of the 13th International Conference on Medical Image Computing and Computer Assisted Intervention (MICCAI 2010), actually none of the high-ranking methods was a purely feature-based method. However, a few of them, including the winner [19] of the online-contest, were hybrid methods, combining intensity with feature-based registration. The feature part of those hybrid methods will also be discussed in this chapter. Table 5.1 contains an overview of feature-based and hybrid non-rigid registration approaches for pulmonary applications. In this chapter, we focus on feature-based registration for lung motion estimation and not on the registration of surrounding structures, such as vertebrae and ribs, for which we only give the work of Matsopoulus (item 2 in Table 5.1) as an example. The authors attempt here to achieve a registration of the lung region of interest independent of the breathing phase.
Feature-based registration approaches can provide a natural way to treat motion field discontinuities, for example at the lung pleura, by separate registration of feature sub-sets, e.g., pulmonary structures and ribs. This is similar to a regionally restricted intensity-based registration, but does not require an accurate region segmentation. The problem, however, how to interpolate a dense motion field for the full image domain persists.

Table 5.1 Classification of feature-based registration for pulmonary applications

	Author	Year	Feature	Correspondence	Interpolation
1	C.V. Stewart et al. [32]	2004	Points, lines, and surfaces	Modified ICP	B-spline-based
2	G.K. Matsopoulos et al. [28]	2005	Points: vertebrae, ribs, shoulder	Self organizing maps	RBF (shifted log)
3	M. Urschler and H. Bischof [33]	2005	Surface: lung surface	Shape context	TPS
4	A. Hilsmann et al. [21]	2007	Points: vessel tree bifurcations	Shape context	TPS
5	T. Klinder et al. [24]	2008	Surfaces: lung surf. and inner structures	Shape constrained deformation	TPS
6	Y. Huang et al. [22]	2009	Points, and lines: bronchial tree, bifurcation points	Hufman code	TPS and Demons
7	V. Gorbunova et al. [17]	2009	Lines, surfaces: vessel tree, lung surface	Currents-based registration	Gaussian kernel diffeomorphic matching
8	K. Cao et al. [6]	2010	Lines: vessel tree	Via hybrid registration	Via hybrid registration
9	D. Loecks et al. [25]	2010	Points: vessel bifurcations	Local and global correspondence model	Via hybrid registration
10	X. Han [19]	2010	Points: Förstner operator	SURF descriptor	Via hybrid registration

5.2 Feature Types

Feature-based registration does not necessarily mean that a point-wise correspondence between landmarks is established, meaning that at the landmark position all degrees of freedom (DOF) for the deformation field are removed. By registration of line-like features such as vessels or bronchial branches only DOF across the line are removed. This leaves one DOF along the line. Similarly, surfaces like the pleura or the lung fissures locally remove only one DOF and leave two DOF on the surface. However, even in the case of line or surface features, often in a successive step, a virtual point-to-point correspondence is established with suitable mapping approaches, such as the iterative closest point (ICP) or related algorithms [3, 12]. Features may be determined as anatomical objects, or by their gray value structure, independent from the anatomy. Examples are, e.g., a bronchial or vascular bifurcation point, or a point with high gray value variability in all three spatial directions.

5.2.1 Anatomical Features

If an anatomical feature can be identified in both images as a unique anatomical landmark, the correspondence problem becomes trivial. In addition, anatomical features are easy to handle in interactive definition or correction schemes. For the registration of the thorax, anatomical objects surrounding the lungs, such as vertebrae and ribs can be used if an independence from the breathing phase is [28] intended. For the estimation of pulmonary motion, however, the surface of the lungs, fissures, bronchial and vascular tree can be used.

Regarding the lung surface, it can be assumed that the motion of it, can to some extent serve as a predictor of the internal lung motion. This is especially the case in the region around the diaphragm. Furthermore, most of the intensity based registration algorithms need as input a delineation of the lungs in order to properly handle the motion discontinuities at the lung borders. While automated lung segmentation is a fairly easy task (at least in the absence of gross pathologies), it is less straight forward to establish anatomical correspondence on the lung surface. In Sects. 5.3.4, 5.3.5, and 5.3.6 approaches to solve the correspondence problem for the lung surface will be discussed.

Further candidates are bronchi and blood vessels. The distal portions of bronchial and vascular trees in the lungs are inaccessible for anatomical identification due to inter-patient variability, the obscuring influences of noise and image artifacts, and the sheer amount of structures such as small branches or bifurcations. Still, these structures can be detected and used as input for feature-based registration.

A weak feature influence within a hybrid registration method was introduced by Cao et al. [6], by adding a 'vesselness'-based [13] similarity measure. With weak in this context we mean that no explicit point-to-point correspondence is established. The approach increases the probability that vessels are registered to vessels, without the need to establish explicit correspondence between the vessel trees to be matched. The additional similarity measure follows Frangi's proposal of using the Eigenvalues of the Hessian matrix to extract curvi-linear image structures in 2D and 3D images. The approach is on the borderline between feature based and intensity based registration. It can be argued that just an additional similarity measure is introduced in an intensity based registration algorithm and that no explicit correspondences are established. On the other hand, image regions are treated differently, depending on the appearance of vessel-like features. Loeckx et al., again in the context of a hybrid registration approach, determined a set of corresponding vessel bifurcation points in fixed and moving image and used them in an additional similarity measure [25]. In a pre-processing step, a set of bifurcations points is generated in both images using a threshold-based segmentation and sub-sequent skeletonization of the pulmonary vessel tree. In addition, the correspondence between the bifurcation points in both images is established (see Sect. 5.3). During the iterations of the hybrid registration, the Euclidean distance between bifurcation points in the fixed image and transformed corresponding points in the moving image is used in addition to a mutual information-based similarity measure.

5.2.2 Gray Value Structure Features

In contrast to anatomically motivated features, it is also possible to search for gray value structures that are on the one hand characteristic enough to allow a good localization and that on the other hand provide a better lung coverage in the distal regions of bronchial and vascular tree. A standard approach for this idea is the analysis of the gradient structure of a small image region, as given by an averaged structure tensor. The structure tensor is the tensor product of the image gradient ∇I with itself. The Eigenvalues of the averaged structure tensor $C = \overline{\nabla I \, (\nabla I)^T}$ are characteristic for the type of structure in the covered region as depicted in Fig. 5.1. Three Eigenvalues that are large in magnitude are required for a characteristic landmark, because this indicates intensity variation in all directions. Consequently, a variety of formulas based on the product of the Eigenvalues of C as given by the determinant, by the sum of the Eigenvalues as given by the trace of C have been proposed as feature point detectors (see [20] for an overview and comparison). Han [19] determined local maxima of the structure tensor-based Förstner operator $det(C)/trace(C^{adj})$ [20] as feature points and established point correspondence using SURF descriptors [1] (see Sect. 5.3). In a hybrid registration setup, the quadratic distance between the resulting feature-based transformation field and the current estimated transformation field was used in addition to a mutual information and a curvature penalizing term during the hybrid registration iterations.

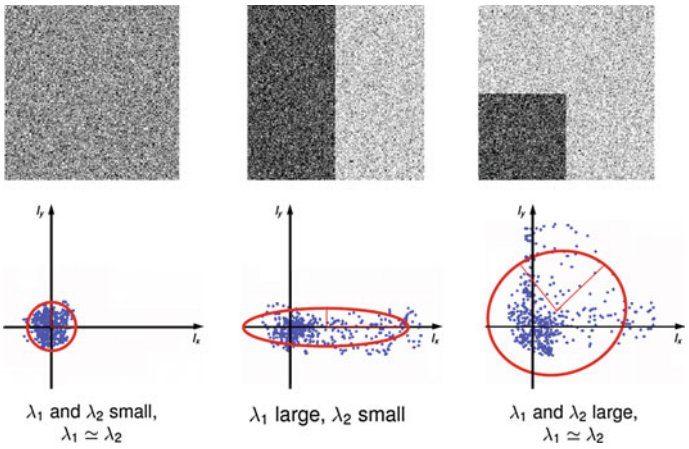

Fig. 5.1 Illustration of the structure tensor for three artificial 2D cases with (i) no predominant (*left*), (ii) one predominant (*middle*), and (iii) two predominant (*right*) gradient directions. The Eigenvectors and values λ_i of the structure tensor can be interpreted as direction and length of the principal axes of an ellipsoid fitted to the distribution. Figure from Goldlücke [16]

5.3 Feature Correspondence

In the case of unique anatomical landmarks, the feature correspondence is trivially given. If this is not the case, correspondence has to be either explicitly established in an additional processing step or implicitly, e.g., by combining the feature-based procedure with an intensity-based registration into a hybrid registration approach. Often, even for named line or surface features, where correspondence of the whole anatomical structure is given, a point-wise correspondence between point sets distributed on the pair of lines or surfaces is established. The main approaches for establishing correspondence are described in the following.

5.3.1 Iterative Closest Point and Modifications

The iterative closest point (ICP) was initially presented by Besl in [3]. Its main idea is to establish a correspondence between two point clouds P and X by performing the following four steps (i) compute for each $\mathbf{p}_i \in P$ the closest point from X, (ii) compute a transformation to match P to X, (iii) apply the transformation to all points in P, (iv) repeat (i)–(iii) until convergence. Initially, it was assumed that the transformation between the two point clouds could be described by a rigid transformation so that step (iii) could be found in a closed form solution. It has to be noted that X does not necessarily have to be a discrete point cloud but could also be a line or surface. Various extensions have been presented to allow non-rigid transformations between the two point clouds (see e.g., [12]). Although the ICP states a very standard algorithm for finding a correspondence between two point sets as it is fast and accurate in many cases, it is a method minimizing a non-convex cost function, and thus it lacks in terms of robustness w.r.t. the initial transformation because of local minima. Furthermore, the computation time is proportional to the number of points, which can be prohibitive when registering two large sets of points. For that reason, many approaches exist addressing robustness, e.g., using a random sampling of points at each iteration, bidirectional distance measurements, remove outliers, or introducing probabilities, and speed, e.g., using k-d trees and/or closest point caching. However, even with latest modifications, robustness and speed are still critical when applying the ICP.

5.3.2 Shape-Based Descriptors

The 'Robust Tree Registration' approach described by Loeckx et al. [25] uses the distance between corresponding vessel tree bifurcation points as an additional similarity measure in a hybrid registration approach. Correspondence is established by means of internal distances between any pair of points. Two distance measures, namely Euclidean and Geodesic distance (shortest path along the tree skeleton) are used

separately. Using a Gaussian distribution model, a distance-based matching probability $P(C_{(i,j).(k,l)})$ is calculated for the occurrence $C_{(i,j).(k,l)}$, that two point-pairs $g_{1,ij}$ and $g_{2,kl}$ found in fixed and moving image respectively, do match.

$$P(C_{(i,j).(k,l)}) = \frac{1}{\sqrt{2\pi\sigma^2}} exp\left(-\frac{\left\|g_{1,ij}, g_{2,kl}\right\|^2}{\sigma^2}\right) \tag{5.1}$$

By marginalization, matching probabilities for any two points in fixed and moving image can be found:

$$P(C_{i,k}) = \sum_j \sum_l P(C_{(i,j).(k,l)}) = m_{G,ik} \tag{5.2}$$

The authors calculate Geodesic $m_{G,ik}$ and Euclidean $m_{E,ik}$ probabilities according to (5.2) and additionally a gray value-based correspondence probabilitiy (see next sub-Sect.). The product of the three is used to finally establish hard correspondences between feature points in fixed and moving image.

5.3.3 Gray Value Descriptors

The 'Robust Tree Registration' approach by Loeckx et al. [25], mentioned in the previous section, uses the gray value-based *'n-dimensional Scale-Invariant Feature Transform'* (*n-SIFT*) descriptor [8] in addition to a shape-based descriptor. The *n-SIFT* descriptor is an extension of the 2-dimensional SIFT descriptor introduced by Lowe [27]. The SIFT approach addresses feature localization as well as feature description. For feature localization, a resolution (scale) pyramid of Gaussian blurred images is created. 'Difference-of-Gaussian' (DoG) images are created by subtracting images of neighboring scales. Feature points are selected as local maxima (in space and scale) in the DoG images. The local orientation is determined based on a gradient orientation histogram around the feature point (see Fig. 5.2 for illustration). The described procedure delivers localization, orientation and scale of a feature point. The final feature description adds information about the local neighborhood of the feature point. First, the image gradient magnitudes and orientations are sampled around the feature point. To achieve orientation invariance, the gradient orientations are rotated relative to the feature point orientation. In order to avoid discontinuities of the descriptor for even small position changes and to give less emphasis to gradients that are far from the feature point, a Gaussian weighting function is used to assign a weight to the magnitude of each sample point. The weighted gradient magnitudes are collected block-wise in orientation histograms. The final descriptor is a vector containing the values of all the orientation histogram entries. In [25], the orientation histogram-based feature descriptor is taken instead of the DoG-based point selection to determine the correspondence between bifurcations in fixed and moving image.

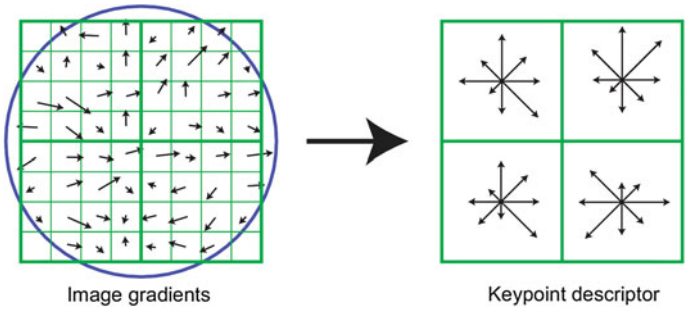

Fig. 5.2 Depiction of the gradient histogram based keypoint descriptor of the SIFT approach [27]. Image gradients (*left*) are weighted by a Gaussian window (*blue circle*) and are accumulated into orientation histograms summarizing the content of a subregion (*right*). The *arrow* length depicts the sum of the gradient magnitudes of the respective directional bin. The figure shows the case of a 2×2 descriptor array computed from an 8×8 set of samples. Figure from Lowe [27]

A cubic volume around each bifurcation is partitioned into 64 blocks and the gradient information is captured in a 60 bin histogram resulting in a 3840 dimensional feature vector. The feature descriptors are used in a probabilistic framework with the probability of correspondence between two bifurcations i and k modeled as Gaussian function:

$$P(i,k) \sim e^{-\|f_i - f_k\|^2}. \tag{5.3}$$

With f_i and f_k being the feature descriptor vector for bifurcation i and k, and $\|\|$ being the magnitude of the difference vector.

The so-called *SURF* features, for 'Speed-Up Robust Features' [1] follow a similar line of thinking. In order to speed up the computation, *SURF* features are based on 'Integral Images' instead of a resolution pyramid of smoothed images. 'Integral Images' give for each pixel position the sum (integral) of image intensities of the image block spanned between image origin and pixel position. They allow the fast computation of approximated blurred derivatives using box-filters. Instead of local maxima of the DoG as in the case of *SIFT*, an approximated determinant of the Hessian matrix is used as detector of blob-like structures to localize feature points. The *SURF* descriptor captures information of the local neighborhood using first order Haar wavelets (see, e.g., [9]) responses, which again can be computed efficiently using the Integral Image. As in the *SIFT* case, image information is captured block wise around the feature point. Denoting the wavelet response in x, y, and z-direction with d_x, d_y, and d_z respectively, the feature descriptor for the ith block is given by the sum of responses within the block:

$$v_i = \left(\sum d_x, \sum d_y, \sum d_z, \sum |d_x|, \sum |d_y|, \sum |d_z|\right) \tag{5.4}$$

The feature descriptors for all blocks are concatenated to produce the total feature descriptor. The *SURF* descriptor was used by Han [19], however for feature points

selected using the Förstner operator (see Sect. 5.2.2). Han used 64 blocks covering a cubic region, resulting in a 384 dimensional feature vector. Correspondences between feature points in fixed and moving image were found using nearest neighbors in the feature space. The inventors of the *SURF* descriptor claim that it combines high quality in terms of repeatability, distinctiveness, and robustness, with high computational performance. For application to pulmonary CT images this is supported by the fact that Han had won the online 'EMPIRE' registration contest within the MICCAI 2010 Workshop 'Medical Image Analysis For The Clinic—A Grand Challenge' [34] while having presented one of the fastest solutions with approx. 10 min computation time per case. It is, however, difficult to determine the portion of success that related to using the *SURF*, since Han used a hybrid approach and further information concerning the contribution of the individual parts of the approach is not available.

5.3.4 Shape Context

The 2D shape context as a regional descriptor of shape was introduced by Belongie et al. [2]. Assume a 2D shape is described by the set of its contour points. Then the idea of the Shape Context is to characterize a location on the contour by assessing in which view directions and in which distance other points on the contour appear. In order to do so, a log-polar histogram is positioned at a reference point on the objects contour and the number of remaining contour points is counted per histogram bin which gives a feature vector representing the shape at the reference point. The 3D shape context [14] is a straightforward extension of the 2D shape context being a 3D spherical histogram H_i in which the displacement vectors from the reference point p_i to the other points are counted. With K denoting the number of bins in the shape context histogram, Urschler and Bischof [33] use a cost function of the form

$$C\left(p_i, p_j\right) = \frac{1}{2}\sum_{k=1}^{K}\frac{\left[h_i(k) - h_j(k)\right]^2}{h_i(k) + h_j(k)} \tag{5.5}$$

to assess whether a point p_i on one shape instance of the lung surface corresponds to a point p_j on another shape instance. The same idea can be applied to a point set representing the centerlines of a tree structure. This allows to establish correspondence between branching points of vessel trees [21] or bronchial trees [5].

5.3.5 Shape Constrained Deformation

The key idea of shape constrained deformation to establish feature correspondence is to adapt a triangulated surface mesh from one image to the other. During the iterative adaptation, an external force attracts the mesh vertices to image features, while an internal force regularizes the attraction by preserving similarity. The topology remains unchanged. The sparse motion field is then derived from the displacement

of corresponding vertices. In contrast to other techniques for feature correspondence, the shape constrained deformation as well as the Shape Context, take into account the topology of the underlying structure and does not treat the feature points as an unconnected set.

5.3.5.1 Lung Surface Generation

The shape constrained deformation relies on the definition of a triangulated surface mesh in one image. In order to not only determine the deformation on the outer surface of the organ, internal structures should also be covered by the surface. In the context of motion field estimation of the lungs, *patient-specific* triangulated surfaces of the lungs are automatically generated in one image which contain most parts of the vessel tree and tumor surfaces. After applying a lung segmentation, all other structures besides the lungs are removed and a triangulation is applied after thresholding the segmented image. Triangulation is thereby performed using marching cubes [26]. Finally, the mesh is post-processed by applying several mesh operations to obtain a smooth surface with a certain amount of triangles, as shown in Fig. 5.3.

5.3.5.2 Mesh Adaptation

Shape-constrained deformation was proposed in [36] and applied for motion estimation in [24, 35]. Using a physical metaphor, the vertex configuration $\mathbf{v}$ that minimizes the following functional of summed energies is computed in each iteration

$$E(\mathbf{v}) = E_{\text{ext}}(\mathbf{v}) + \alpha E_{\text{int}}(\mathbf{v}). \tag{5.6}$$

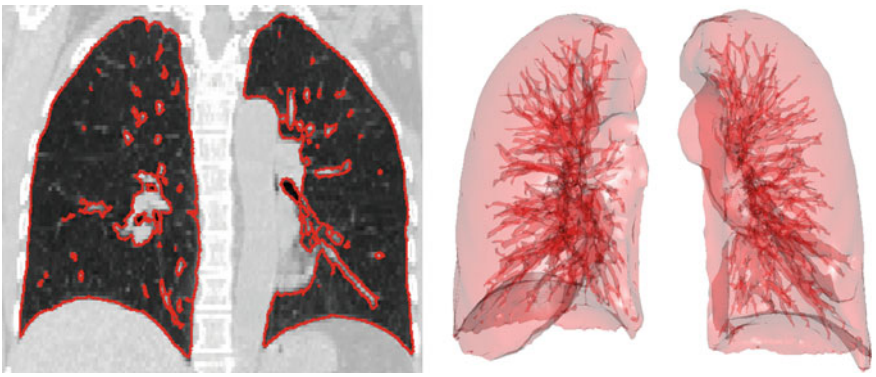

Fig. 5.3 Surface mesh capturing the transition from lung parenchyma to the lungs wall and to lung internal structures, such as vessels and bronchi. The mesh is shown in a coronal cut-plane (*left*) and as surface rendering (*right*). Shape constrained deformation allows to track the mesh through the breathing cycle, keeping mesh vertices at anatomically corresponding points

The parameter α balances the influence of both energy terms.

The external energy drives the mesh towards detected candidates by performing a feature search in a local neighborhood around the surface. Feature search is realized in a discrete manner by searching via a predefined sample pattern. For each barycenter of a triangle $\hat{\mathbf{x}}_i$, feature search is carried out in the direction of its normal $\mathbf{n}_i$

$$\mathbf{c}_j = j\delta\mathbf{n}_i \quad \text{with} \quad j = -l, \ldots, l, \tag{5.7}$$

which results in $(2l + 1)$ discrete sampling points $\mathbf{c}_j$, with a distance of δ. At every sampling point $\mathbf{x}_i^j = \hat{\mathbf{x}}_i + \mathbf{c}_j$, a feature function is evaluated and finally the target point is chosen best combining the feature value $F(.)$ and the distance $j\delta$ to the barycenter of the triangle

$$\mathbf{x}_i^{\text{target}} = \min_{\mathbf{x}_i^j \,|\, j=-l,\ldots,l} \left\{ Dj^2\delta^2 - F(\mathbf{x}_i^j) \right\} \tag{5.8}$$

with the weighting factor D.

With the detected target points $\mathbf{x}_i^{\text{target}}$, the external energy is given in a quadratic form as

$$E_{\text{ext}}(\mathbf{v}) = \sum_i w_i \left(\frac{\nabla I(\mathbf{x}_i^{\text{target}}) \nabla I(\mathbf{x}_i^{\text{target}})^T}{\left\| \nabla I(\mathbf{x}_i^{\text{target}}) \right\|^2} (\mathbf{x}_i^{\text{target}} - \mathbf{M}_i\mathbf{v}) \right)^2, \tag{5.9}$$

where $\mathbf{M}_i$ expresses the vertices $\mathbf{v}$ in terms of triangle centers and w_i is a weighting factor. The projection of $(\mathbf{x}_i^{\text{target}} - \mathbf{M}_i\mathbf{v})$ onto the image gradient at the target position $\nabla I(\mathbf{x}_i^{\text{target}})$ makes the energy invariant to movements of the triangle within the object tangent plane, thus preventing the triangle from becoming stuck at the target position. The weights w_i in Eq. (5.9) can be chosen according to the feature value of the target points to give the most promising points the largest influence during mesh reconfiguration.

Attraction of the mesh vertices to image features is accomplished by evaluating a certain feature function given as:

$$F(\mathbf{x}_i^j) = s \cdot \mathbf{n}_i^T \nabla I(\mathbf{x}_i^j) \frac{e^{\frac{\left\| \nabla I(\mathbf{x}_i^j) \right\|}{g_{\max}}}}{1 + \frac{\left\| \nabla I(\mathbf{x}_i^j) \right\|}{g_{\max}} e^{\frac{\left\| \nabla I(\mathbf{x}_i^j) \right\|}{g_{\max}}}}, \tag{5.10}$$

where the parameter $s \in \{1, -1\}$ accounts for the gradient direction, and $\mathbf{n}_i$ is the normal of the triangle for which the feature search is carried out. The gradient response is bounded by some threshold $g_{\max}$.

In order to distinguish between edges with similar feature responses further image quantities, as e.g., gray value statistics along the edge, have to be considered. For

Table 5.2 Registration accuracy for 5 publicly available image pairs at end of exhale and inhale breathing phase [7]

		Case 1	Case 2	Case 3	Case 4	Case 5
Without	$\mu \pm \sigma$	3.89 ± 2.78	4.34 ± 3.90	6.94 ± 4.05	9.83 ± 4.86	7.47 ± 5.51
registration	max	10.90	17.69	16.55	20.25	24.77
SCD	$\mu \pm \sigma$	1.01 ± 0.55	1.10 ± 0.53	1.33 ± 0.79	1.62 ± 1.16	1.70 ± 1.30
	max	3.42	3.47	5.19	12.39	16.54
Currents	$\mu \pm \sigma$	1.44 ± 0.72	1.72 ± 1.38	2.97 ± 2.96	3.30 ± 2.61	3.52 ± 2.91
FEIR	$\mu \pm \sigma$	1.02 ± 0.50	1.04 ± 0.50	1.44 ± 0.94	1.60 ± 1.32	1.67 ± 1.53
	max	2.77	3.40	7.31	13.26	15.92

The target registration error (TRE) for 300 manually placed landmarks, also provided by the study is presented. The Table lists mean, max, and std. dev. values of the TRE in mm resulting from two feature-based registration techniques: *Shape constrained deformation* (SCD, see Sect. 5.3.5), and *Currents* (see Sect. 5.3.6), and one intensity based registration technique: *Fast elastic image registration* (FEIR [23]). SCD and FEIR result in very similar TREs. The Currents based approach results in slightly higher values.

this reason, rejection intervals can be defined so that the feature will not be evaluated if certain image quantities, q^k, violate some learned criteria

$$\tilde{F}(\mathbf{x}_i^j) = \begin{cases} F(\mathbf{x}_i^j) : q^k \in [q^k_{\min}, q^k_{\max}] & \text{for all } q^k \text{ in } S \\ 0 \quad\quad\;\; : q^k \notin [q^k_{\min}, q^k_{\max}] & \text{for some } q^k \text{ in } S \end{cases}, \tag{5.11}$$

where S is the set of considered quantities.

Penalizing a deviation of the model's shape regularizes the image forces acting on it, and decreases the attraction to false image features. The internal energy

$$E_{\text{int}}(\mathbf{v}) = \sum_{j \in V} \sum_{k \in N(j)} ((\mathbf{v}_j - \mathbf{v}_k) - (\mathcal{T}_{\text{int}}[\mathbf{m}_j] - \mathcal{T}_{\text{int}}[\mathbf{m}_k]))^2 \tag{5.12}$$

preserves the shape similarity of all adapted vertices $\mathbf{v}_j$ to the model vertices $\mathbf{m}_j$, with $N(j)$ being the set of neighbors of the vertex with index j. Deviations from the initial model are penalized by calculating the vector difference between neighboring vertices of the adapted mesh and the corresponding vertices of the shape model undergoing a geometric transformation $\mathcal{T}_{\text{int}}[.]$. Depending on the desired flexibility of the underlying shape prior, similarity transformations or affine transformations are typically chosen. In each case, the geometric transformation is determined prior to the calculation of Eq. (5.12) in a closed form solution based on the point correspondences between adapted and model vertices.

Table 5.2 shows the target registration error (TRE) for 5 publicly available inhale/exhale image pairs [7] in comparison to the Currents based approach, discussed in the next chapter, and to an intensity based image registration approach [23].

5.3.6 Currents-Based Registration

Another approach, using so called currents, to circumvent explicit correspondences was used by Gorbunova et al. in [17]. The basic idea is to represent shapes as sets of vectors: Tangential vectors in the case of curvi-linear shapes and normal vectors in the case of *surfaces* (see [11] and references therein). The *current* associated with a surface is defined as the flux of a probing vector field ω through the surface S:

$$S(\omega) = \int_S \omega(\mathbf{x})^t (\mathbf{u} \times \mathbf{v})(\mathbf{x}) d\sigma(\mathbf{x}) \tag{5.13}$$

where $(\mathbf{u}, \mathbf{v})$ is a local basis of its tangent plane at $\mathbf{x}$, $(\mathbf{u} \times \mathbf{v})(\mathbf{x})$ being the surface normal at $\mathbf{x}$ and $d\sigma(\mathbf{x})$ the area element of the surface. Similarly, the current associated with a curvi-linear structure L is defined as the path-integral of a probing vector field ω along the curve:

$$L(\omega) = \int_L \omega(\mathbf{x})^t \tau(\mathbf{x}) \mathbf{dx} \tag{5.14}$$

with $\tau(\mathbf{x})$ being the tangent of the curve at $\mathbf{x}$. Figure 5.4 depicts the currents representing a pulmonary vessel tree. We adhere to the notation of the authors of [11] by using the same letters L and S for the geometrical structure and their associated currents. So currents are a mapping of the space of vector fields ω to the space of real numbers $\mathbb{R}$. This provides the basis to define a similarity measure in the context of the registration of curves, surfaces, or sets of them. Simplified, to register the surfaces S_1 and S_2, the idea is to evaluate the flux integral Eq. (5.13) through S_1 using a probing vector field constructed from S_2 and vice versa. To be able to do this efficiently, the vector fields ω are represented as an integral (or sum in the discrete case) of reproducing Gaussian kernels $K^W(\mathbf{x}, \mathbf{y}) = exp(- \parallel \mathbf{x} - \mathbf{y} \parallel^2 \lambda_w^2)$. $\mathbf{x}, \mathbf{y}$ are the positions and λ_W the width of the kernel. Given a vector β at position $\mathbf{y}$, the

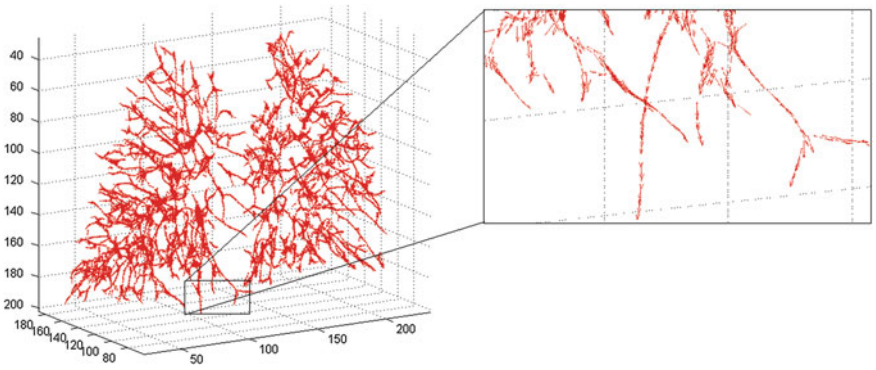

Fig. 5.4 Currents corresponding to pulmonary vessel centerlines. Figure from Gorbunova et al. [17]

corresponding vector field is given by $\omega(\mathbf{x}) = K^W(\mathbf{x}, \mathbf{y})\beta$, the vector field of a set of local vectors is the superposition of the individual contributions. Representing curves and surfaces as piecewise linear structures (e.g. as polygons, or triangular meshes, respectively), each element (a straight line element, or a triangle, respectively) gives rise to a reproducing kernel positioned at the center of that element. In the formalism above, the distance between two curves or two surfaces can be calculated without the need for establishing point-wise correspondence between the two structures. This is achieved by a distance metric using a kernel-based inner product of currents:

$$\langle L, L^{'} \rangle = \sum_{i=1}^{n} \sum_{j=1}^{m} (\tau_i)^t K^W(\mathbf{c}_i, \mathbf{c}_j^{'}) \tau_j^{'}, \tag{5.15}$$

where L and $L^{'}$ are the two curves to be matched, with a number of n and m line-elements, and with tangential vectors τ_i and $\tau_j^{'}$, and centers $\mathbf{c}_i$ and $\mathbf{c}_j^{'}$ respectively. So the term $(\tau_i)^t K^W(\mathbf{c}_i, \mathbf{c}_j^{'})\tau_j^{'}$ measures the match of tangential vectors of the line elements. The distance between the two curves L and $L^{'}$ is then

$$d^2(L, L^{'}) = \| L^{'} - L \|^2 = \| L \|^2 + \| L^{'} \|^2 - 2\langle L, L^{'} \rangle, \tag{5.16}$$

with the norm of a current L, $\| L \|$ being defined as the supremum path integral of any regular vector field. The registration of the curves L and $L^{'}$ is performed in the framework of large deformation diffeomorphic matching [15] with a cost function combining the distance for line, and surface features, and a regularization term advancing smoothness of the resulting transformation field. Currents-based registration of lung images has been recently introduced. Results reported so far (see 5.2) do not completely reach the accuracy of intensity-based registration, but possibly the advantages of the approach have not been completely exploited yet. Recently, a hybrid registration approach using currents has been presented [18].

5.4 Interpolation

Finally, to be able to obtain deformation vectors between feature points, an interpolation of the sparsely given deformation field is required. In the following sub-Sections a selection of proposed methods will be discussed.

5.4.1 B-Splines

B-spline-based approaches are very efficient when a sparse set of deformation vectors defined on a Cartesian grid shall be interpolated, see e.g. Rueckert et al. [31].

McClelland used B-spline interpolation to create a 4D motion model in [29]. Since in our case, feature points are virtually always irregularly distributed and since B-spline-based interpolation is described in some detail in Chap. 6.2.1, we omit a description here.

5.4.2 Radial Basis Functions

Radial basis functions perform an interpolation of the sparse and possibly irregularly defined deformation by expressing the deformation as a linear combination of the sparse deformation weighted by some kernel. One common way to perform the interpolation is by using thin-plate splines (TPS) [4]. The TPS approach is physically motivated by a thin metal plate which will take the overall shape in which it is least bent given the deformation at some locations. The approach can be generalized to arbitrary dimensions d and degrees of smoothness in terms of the order m of derivatives of the associated functional to be minimized [30]. For the physically motivated case of minimal bending energy, we have $m = 2$. The radial basis functions $U(\mathbf{x}, \mathbf{p})$ associated to the respective choice of d and m are

$$U(\mathbf{x}, \mathbf{p}) \sim \begin{cases} |\mathbf{x} - \mathbf{p}|^{2m-d} \, ln|\mathbf{x} - \mathbf{p}|, & \text{if } (2m - d) \text{ is an even positive integer} \\ |\mathbf{x} - \mathbf{p}|^{2m-d}, & \text{otherwise} \end{cases} \tag{5.17}$$

In contrast to TPS, elastic-body splines (EBS) [10] use a more sophisticated physical model derived from the Navier partial differential equations for a homogeneous isotropic elastic body subjected to loads (forces)

$$\mathbf{f}(\mathbf{x}) = \mu \nabla^2 \mathbf{u}(\mathbf{x}) + (\lambda + \mu) \nabla (\nabla \cdot \mathbf{u}(\mathbf{x})) \tag{5.18}$$

where $\mathbf{u}(\mathbf{x})$ is the displacement of a point, ∇^2 denote the Laplacian and ∇ the gradient, $\nabla \cdot \mathbf{u}(\mathbf{x})$ is the divergence and $\mathbf{f}(\mathbf{x})$ is the force field. Typically, for the three-dimensional case, the radial kernel for the EBS that defines the force field is chosen as $r(\mathbf{x}) = (x + y + z)^{\frac{1}{2}}$. The Lamé coefficients λ and μ allow to describe the physical properties of the elastic material. Both TPS and EBS lead to an equation of the type

$$\mathbf{d}(\mathbf{x}) = \sum_i \mathbf{U}(\mathbf{x}, \mathbf{p}_i)\mathbf{c}_i + \mathbf{A}\mathbf{x} + \mathbf{b} \tag{5.19}$$

expressing the deformation vector $\mathbf{d}$ with an affine part $\mathbf{A}\mathbf{x} + \mathbf{b}$ and a weighted sum of radial basis functions $U(\mathbf{x}, \mathbf{p}_i)$. Weights $\mathbf{c}_i$ are determined using the condition that Eq. (5.19) is fulfilled for all point-pairs $\mathbf{p}_i$ and $\mathbf{q}_i$ in fixed and moving image, respectively. This condition leads with $\mathbf{d}_i = \mathbf{q}_i - \mathbf{p}_i$ to a linear equation system which can be solved with standard approaches, such as the Singular Value Decomposition. In case of EBS, equations are coupled with respect to space coordinates. The TPS equations, associated with displacements along one coordinate axis, are independent.

Therefore, the computational effort for EBS is higher limiting the use of EBS. For many applications, TPS provide a sufficient model and can be computed with reasonable computational effort and they are thus the method of choice. However, as the radial basis function-based interpolation is defined as a linear combination of the sparse deformation weighted by some kernel, the deformation at one location $\mathbf{x}$ is influenced by *all* given displacement vectors of the sparse deformation field, i.e., in other words the impact of some displacement vectors of the sparse deformation field is not only local but global. Thus, as all displacement vectors of the sparse deformation field have to be considered, the radial based interpolation can result in high computational costs once the number of given displacement vectors becomes large.

5.4.3 Nearest Neighbour Interpolation

The idea of a K nearest neighbour (KNN) interpolation is to find the dense deformation by taking the K nearest locations with sparse motion vectors $\mathbf{u}_k$ for a given position $\mathbf{x}$ and then calculate the deformation as

$$\mathbf{u}_\mathbf{x} = \frac{1}{\sum_{k=1}^{K} w_k} \sum_{k=1}^{K} w_k \mathbf{u}_k \tag{5.20}$$

where $\mathbf{u}_\mathbf{x}$ is the deformation vector at position $\mathbf{x}$ and w_k is a weighting factor. If w_k is equal to one, then the mean is calculated. However, the w_k can also be defined to be distance dependant, so that $\mathbf{u}_k$ that belong to locations that lie further away from $\mathbf{x}$ have less influence. In contrast to other interpolation schemes, the KNN interpolation does not assume a physical model. Especially, when a large number of sparse locations is given, computation of, e.g., radial basis function-based interpolation, can be computationally very expensive. However, the problem of KNN is that the interpolation is not smooth which can lead to a locally implausible deformation field and, e.g., Gaussian-smoothing is needed to overcome this limitation. Comparing lung motion fields interpolated motion fields using TPS and KNN interpolation, showed that TPS provided a higher landmark accuracy [35].

References

1. Bay, H., Ess, A., Tuytelaars, T., Van Gool, L.: Speeded-up robust features (surf). Comput. Vis. Image Underst. **110**, 346–359 (2008)
2. Belongie, S., Malik, J., Puzicha, J.: Shape matching and object recognition using shape contexts. IEEE Trans. Pattern Anal. Mach. Intell. **24**(4), 509522 (2002)
3. Besl, P.J., McKay, N.D.: A method for registration of 3-d shapes. IEEE Trans. Pattern Anal. Mach. Intell. **14**, 239–256 (1992)

4. Bookstein, F.: Principal warps: thin-plate splines and the decomposition of deformations. IEEE Trans. Pattern Anal. Mach. Intell. **11**(6), 567–585 (1989)
5. Buelow, T., Lorenz, C., Wiemker, R., Honko, J.: Point based methods for automatic bronchial tree matching and labelling In: Proceedings of SPIE Conference on Medical Imaging: Physiology and Function from Medical Images, vol. 6143, pp. O1430. San Diego (2006)
6. Cao, K., Du, K., Ding, K., Reinhardt, J.M., Christensen, G.E.: Regularized nonrigid registration of lung ct images by preserving tissue volume and vesselness measure. In: van Ginneken, B. Murphy, K., Heimann, T., Pekar, V., Deng, X. (eds.) MICCAI2010 Workshop: Medical Image Analysis For The Clinic–A Grand Challenge, pp. 43–54. CreateSpace (2010)
7. Castillo, R., Castillo, E., Guerra, R., Johnson, V.E., McPhail, T., Garg, A.K., Guerrero, T.: A framework for evaluation of deformable image registration spatial accuracy using large landmark point sets. Phys. Med. Biol. **54**(7), 18491870 (2009)
8. Cheung, W., Hamarneh, G.: n-sift: n-dimensional scale invariant feature transform. IEEE Trans. Image Process. **18**, 2012–2021 (2009)
9. Chui, C.K.: An Introduction to Wavelets. Academic Press, San Diego (1992)
10. Davis, M., Khotanzad, A., Flamig, D., Harms, S.: A physics-based coordinate transformation for 3-d image matching. IEEE Trans. Med. Imaging **16**(3), 317–328 (1997)
11. Durrleman, S., Pennec, X., Trouvé, A., Thompson, P., Ayache, N.: Inferring brain variability from diffeomorphic deformations of currents: an integrative approach. Med. Image Anal. **12**(5), 626–637 (2008)
12. Feldmar, J., Declerck, J., Malandain, G., Ayache, N.: Extension of the icp algorithm to nonrigid intensity-based registration of 3d volumes. Comput. Vis. Image Und. **66**(2), 193–206 (1997)
13. Frangi, A.F., Niessen, W.J., Vincken, K.L., Viergever, M.A.: Muliscale vessel enhancement filtering. In: Medical Image Computing and Computer-Assisted Intervention (MICCAI 1998). Lecture Notes in Computer Science **1496**, 130–137 (1998)
14. Frome, A., Huber, D., Kollure, R., Bülow, T., Malik, J.: Recognizing objects in range data using regional point descriptors. In: Proceedings of ECCV, pp. 533540 (2004)
15. Glaunes, J., Qiu, A., Miller, M.I., Younes, L.: Large deformation diffeomorphic metric curve mapping. Int. J. Comput. Vis. **80**(3), 317–336 (2008)
16. Goldlücke, B.: The Structure Tensor of an Image. In: Lecture: Introduction to Image Processing on the GPU, Heidelberg Collaboratory for Image Processing. http://hci.iwr.uni-heidelberg.de/Staff/bgoldlue/cuda_ss_2012/cuda_ss_2012_01_structure_tensor.pdf (2012)
17. Gorbunova, V., Durrleman, S., Lo, P., Pennec, X., de Bruijne, M.: Curve- and surface-based registration of lung CT images via Currents. In: Proceedings of Second International Workshop on Pulmonary Image Processing, MICCAI, pp. 15–25. London (2009)
18. Gorbunova, V., Durrleman, S., Lo, P., Pennec, X., de Bruijne, M.: Lung CT registration combining intensity, curves and surfaces. In: IEEE International Symposium on Biomedical Imaging: From Nano to Macro, 2010, pp. 340–343 (2010)
19. Han, X.: Feature-constrained nonlinear registration of lung ct images. In: van Ginneken, B., Murphy, K., Heimann, T., Pekar, V., Deng, X. (eds.) MICCAI2010 Workshop: Medical Image Analysis For The Clinic–A Grand Challenge, pp. 63–72. CreateSpace (2010)
20. Hartkens, T., Rohr, K., Stiehl, H.S.: Evaluation of 3d operators for the detection of anatomical point landmarks in MR and CT images. Comput. Vis. Image Und. **86**(2), 118–136 (2002)
21. Hilsman, A., Vik, T., Kaus, M., Franks, K., Bissonette, J.P., Purdie, T., Beziak, A., Aach, T.: Deformable 4D CT lung registration with vessel bifurcations. In: Proceedings of International Conference of Computer Assisted Radiology and Surgery (CARS 2007). Berlin, Germany (2007)
22. Huang, Y., Feng, H., Zhao, P., Tong, T., Li, C.: Automatic landmark detection and norid registration of intra-subject lung CT images. In: International Conference on Information Science and, Engineering, pp. 3605–3608 (2009)
23. Kabus, S., Lorenz, C. : Fast elastic image registration. In: van Ginneken, B., Murphy, K., Heimann, T., Pekar, V., Deng, X. (eds.) MICCAI2010 Workshop: Medical Image Analysis For The Clinic–A Grand Challenge, pp. 81–89. CreateSpace (2010)

24. Klinder, T., Lorenz, C., von Berg, J., Renisch, S., Blaffert, T., Ostermann, J.: 4DCT image-based lung motion field extraction and analysis. In: Proceedings of SPIE Conference on Medical Imaging: Image Processing, vol. 6914, pp. 69, 141L–1-11 (2008)
25. Loeckx, D., Smeets, D., Keustermans, J., Hermans, J., Maes, F., Vandermeulen, D., Suetens, P.: 3d lung registration using splineMIRIT and robust tree registration (RTR). In: B. van Ginneken, K. Murphy, T. Heimann, V. Pekar, X. Deng (eds.) MICCAI2010 Workshop: Medical Image Analysis For The Clinic—A Grand Challenge, pp. 109–117. CreateSpace (2010)
26. Lorensen, W., Cline, H.: Marching cubes: a high resolution 3D surface construction algorithm. Comput. Graph. **21**, 163–169 (1987)
27. Lowe, D.G.: Distinctive image features from scale-invariant keypoints. Int. J. Comput. Vis. **60**, 91–110 (2004)
28. Matsopoulos, G.K., Mouravliansky, N.A., Asvestas, P.A., Delibasis, K.K., Kouloulias, V.: Thoracic non-rigid registration combining self-organizing maps and radial basis functions. Med. Image Anal. **9**(3), 237–254 (2005)
29. McClelland, J.R., Blackall, J.M., Tarte, S., Chandler, A.C., Hughes, S., Ahmad, S., Landau, D.B., Hawkes, D.J.: A continuous 4d motion model from multiple respiratory cycles for use in lung radiotherapy. Med. Phys. **33**(9), 3348–3358 (2006)
30. Rohr, K., Stiehl, H., Sprengel, R., Buzug, T., Weese, J., Kuhn, M.: Landmark-based elastic registration using approximating thin-plate splines. IEEE Trans. Med. Imaging **20**(6), 526–534 (2001)
31. Rueckert, D., Sonoda, L.I., Hayes, C., Hill, D.L.G., Leach, M.O., Hawkes, D.J.: Non-rigid registration using free-form deformations: application to breast mr images. IEEE Trans. Med. Imaging **18**(8), 712–721 (1999)
32. Stewart, C.V., Lee, Y.L., Tsai, C.L.: An uncertainty-driven hybrid of intensity-based and feature-based registration with application to retinal and lung CT images. In: Medical Image Computing and Computer-Assisted Intervention (MICCAI 2004). Lecture Notes in Computer Science **3216**, 870–877 (2004)
33. Urschler, M., Bischof, H.: Assessing breathing motion by shape matching of lung and diaphragm surfaces. In: Proceedings of SPIE Conference on Medical Imaging: Physiology and Function from Multidimensional Images, vol. 5746, pp. 440–452. San Diego (2005)
34. van Ginneken, B., Murphy, K., Heimann, T., Pekar, V., Deng, X. (eds.): MICCAI2010 Workshop: Medical Image Analysis for the Clinic—A Grand Challenge. CreateSpace (2010)
35. von Berg, J., Barschdorf, H., Blaffert, T., Kabus, S., Lorenz, C.: Surface based cardiac and respiratory motion extraction for pulmonary structures from multi-phase CT. In: Proceedings of SPIE Conference on Medical Imaging: Physiology and Function from Medical Images, vol. 6511, pp. 65, 110Y1-11 (2007)
36. Weese, J., Kaus, M., Lorenz, C., Lobregt, S., Truyen, R., Pekar, V.: Shape constrained deformable models for 3D medical image segmentation. In: Proceedings of Image Processing in Medical Imaging (IPMI), pp. 380–387. Springer (2001)